



Fe₃O₄ Templated Pyrolyzed Fe–N–C Catalysts. Understanding the role of N-Functions and Fe₃C on the ORR Activity and Mechanism

Ricardo Venegas,^[a] César Zúñiga,^[a] José H. Zagal,^[a] Alejandro Toro-Labbé,^[b] José F. Marco,^[c] Nieves Menéndez,^[d] Karina Muñoz-Becerra,^{*,[e]} and Francisco J. Recio^{*,[d]}

Pyrolyzed non-precious metal catalysts have been proposed as an alternative to substitute the expensive and scarce noble metal catalysts in several conversion energy reactions. For the oxygen reduction reaction (ORR), the pyrolyzed catalyst M–N–C (M: Fe or Co) presents remarkable catalytic activity in acid and alkaline media. These pyrolyzed materials show a high heterogeneity of active sites being the most active in the MN_x moieties. The activity and stability of these catalysts are also conditioned by other structural parameters such as the area, the N-doping, and by the presence of metal particles. In this study, we explore the use of Fe₃O₄ nanoparticles as templates and as iron sources to synthesize Fe–N–C. The best perform-

ance for the ORR in acidic media was reached with the catalysts using nanoparticles covered by PANI and iron salts as the precursor, with an onset potential of 0.85 vs. RHE and a direct 4-electrons mechanism. We corroborated the use of the catalysts' redox potential as reactivity descriptors and discussed the detrimental role of the presence of Fe₃C metallic particles in the mechanism. Based on the experimental results, we performed DFT calculations to explore the influence of N-doped species on the electronic density of the iron centers of FeN₄ active sites, and we propose a theoretical model for increasing the activity based on the distance and ratio of N-doping to iron center.

Introduction

Energy production without the undesirable generation of CO₂ has become one of the significant challenges for the scientific community. Among the explored alternatives for replacing carbon-based fuels, the polymer-electrolyte membrane fuel

cells (PEMFC) powered by hydrogen have been considered an alternative for electrification in mobility and transport.^[1–3] However, the use of Pt-based catalysts, which are necessary to catalyze the oxygen reduction reaction, is the main weakness for the massification of this technology due to the scarcity and high price of these noble-metal catalysts.^[4,5] Within the search of non-precious metal-based materials with similar activity and durability of Pt-based catalysts, the pyrolyzed M–N–C materials (M = Fe, Co) have been proposed as an alternative due to the good catalytic activity for the ORR in acid and alkaline media and their low price. Their remarkable catalytic activity is associated with the graphitization of the carbon precursors and the insertion of metal and nitrogen atoms into the material that can act as active sites to catalyze the ORR.^[6,7]

Several successful synthetic routes have been proposed in the last decade to optimize the performance of these catalysts. The highest catalytic activities, evaluated from the onset potential, have been found in pyrolyzed catalysts using MOF or other structured compounds as precursors, where the initial structure of the precursor is preserved after the pyrolysis process.^[8] The use of C–N rich conjugated polymers as polyaniline in the synthesis produces catalysts with good stability *in operando* conditions due to their high degree of graphitization.^[9] The use of inorganic templates as silica nanoparticles to increase the final surface area has been explored, the results showing good activity due to the high surface area generated after the etching of the silica nanoparticles (NPs).^[10] In addition, the use of ball-milling instead of solvents has been an advance from the point of view of scalability. The insertion and availability of different active sites in the graphitized

[a] Dr. R. Venegas, Dr. C. Zúñiga, Prof. J. H. Zagal
Facultad de Química y Biología, Universidad de Santiago de Chile, Av. Libertador Bernardo O'Higgins 3363, Santiago, Estación Central, Región Metropolitana, Santiago, Chile

[b] Prof. A. Toro-Labbé
Departamento de Química-Física, Facultad de Química y de Farmacia, Pontificia Universidad Católica de Chile, Av. Vicuña Mackenna 4860, Macul, Región Metropolitana, Santiago, Chile

[c] Dr. J. F. Marco
Instituto de Química Física "Rocasolano" CSIC, Serrano 119, 28006 Madrid, Spain

[d] Dr. N. Menéndez, Dr. F. J. Recio
Departamento de Química Física Aplicada, Facultad de Ciencias, Universidad Autónoma de Madrid, C/Francisco Tomás y Valiente 7, 28049, Madrid, Spain
E-mail: javier.recio@uam.es

[e] Dr. K. Muñoz-Becerra
Universidad Bernardo O'Higgins, Centro Integrativo de Biología y Química Aplicada (CIBQA), General Gana 1702, Santiago, Chile, 8370854
E-mail: kamunozb@uc.cl
karina.munoz@ubo.cl

Supporting information for this article is available on the WWW under <https://doi.org/10.1002/celec.202200115>

An invited contribution to a Special Collection on Current Trends in Electrochemistry 2021 for the 1st French–Spanish Workshop on Electrochemistry

© 2022 The Authors. ChemElectroChem published by Wiley-VCH GmbH. This is an open access article under the terms of the Creative Commons Attribution License, which permits use, distribution and reproduction in any medium, provided the original work is properly cited.

materials have been demonstrated to depend directly on the synthetic route and the used precursors.^[11–13]

From the point of view of the active sites, the pyrolyzed catalysts present high heterogeneity, different N-doping, carbon defects, FeN_x moieties, and secondary metallic particles, which have been proposed as active sites for the ORR.^[13–15] The inserted N atoms in Fe–N–C catalysts have been identified as graphitic, pyrrolic, and pyridinic, while Fe atoms have been mainly described as FeN_x units to which a prevalence as active sites for the ORR have been demonstrated.^[14,16] The mesoporosity and the availability of these active sites, preferably formed over the edges of the graphitic layers, favor the mass transport and hence the ORR activity.^[12,17,18] In addition, other metallic particles as oxide/carbide/nitride nanoparticles are formed during pyrolysis.^[9,19] Nevertheless, the role of these metallic-based nanoparticles in the catalytic process is still not completely clear. Several authors have stated that the ORR activity for Fe–N–C catalyst can be associated with the Fe(III/II) reduction potential as for MN₄ type catalysts^[15,16,20,21] and that in some cases is increased when metallic nanoparticles are in contact and anchored with the graphitic layers.^[15] This effect is associated with the ability of nanoparticles to modify their electronic structure in the same way as when N and/or metallic-based sites are inserted.^[15,22] The ability of iron containing-particles to resist the leaching treatments using acidic media, usually carried out before a second pyrolysis treatment, has been attributed to their coating by protective graphitic layers and achieved during the thermal treatments.^[23,24] For instance, the role in the ORR activity of iron-based carbide particles (Fe₃C) that are usually formed during the pyrolysis treatments^[25] is a controversial matter since, in the literature, they have been described merely as impurities affecting the activity^[26,27] and as carbon-coated particles with a significant synergic influence over the active single FeN₄ sites.^[13,28] Some authors have related their participation in the ORR catalytic performance with promoting the 2×2 electron pathway,^[22,29] while others have stated that their presence efficiently promotes the 4-electron pathway.

The inclusion of Fe₃O₄ as a precursor agent in the synthesis of Fe–N–C materials has been done to prove their influence over the ORR catalytic activity.^[30–32] For instance, the influence of the Fe₃O₄ nanoparticles loading in obtaining Fe₃O₄/N-doped aerogel composites was studied by Wu et al.,^[30] who showed that an increase of the magnetite content in the synthesis from 4.1 to 46.2 wt% results in the enhancing the ORR selectivity in basic media. Additionally, the pyrolysis of a mixture of chemical-synthesized magnetite particles (400 nm) with PANI at 700 °C allows obtaining a high ORR active mesoporous N-doped carbon shell which encapsulates the Fe₃O₄ particles. The onset potential of 0.21 V vs. Ag/AgCl was more positive than that of the physically absorbed Fe₃O₄-PANI and pyrolyzed PANI tested at neutral pH, demonstrating potential applications in microbial fuel cells.^[32] Based on the Fe2p XPS analysis, the authors suggested that the active material accounts by Fe₃O₄ particles only, not showing Fe–N coordination.

The influence of the N-functions content as pyridinic, graphitic and/or pyrrolic for the ORR activity of pyrolyzed

Fe–N–C catalysts has been widely studied experimentally and theoretically.^[14,33–35] Some reports have established that N atoms inserted in graphitized matrices act as soft or intermediate bases (according to the Pearson acid-base principle, HSAB) and as π -acceptor ligands, modifying the electronic density of neighboring atoms as carbon in a graphitized matrix^[36–40] or metal centers as iron in the same way as electron-withdrawing substituents in MN₄ non pyrolyzed^[41] and pyrolyzed macrocycles.^[21] This effect is the opposite of epoxy and hydroxyl groups (oxidized graphene) that act as hard bases and as σ -donor ligands, reducing the electron π -delocalization over the graphitic plane and, in consequence, the dioxygen binding energy.^[42,43] Concerning the influence of N-defects over the conductance degree, Zhang et al. have studied that the inserted N atoms in N-doped graphene materials cause an electronic perturbation over the xy graphitic plane attributed to the sp^2 -N electronic nature that depending on its configuration, have a more or less incidence over the carbonaceous matrix charge distribution (π -delocalization), with a long-range spin density perturbation associated to a higher conductance.^[38] Mechanistically, the N_{graph} functions in the material's surface can reduce the energy barrier for the first ORR electron transfer,^[44,45] while the N_{pyr} functions as Lewis base sites influence over the adjacent carbon atoms turning them into secondary active sites.^[36,46] Nevertheless, these effects have not been studied for Fe–N–C catalysts in terms of the electronic process accompanying the Fe–O₂ adduct formation in the ORR *r.d.s.*

In this work, we explore the role of the Fe₃O₄ NPs as a precursor and template for the synthesis of Fe–N–C pyrolyzed catalysts for the electroreduction of dioxygen in acid media. By the study of C–N precursors, iron source and nanoparticle templates, we obtain catalysts with different compositions and catalytic activity. Among the different active sites characterized in the catalysts, the FeN₄ moieties embedded in the carbon graphitic matrix showed the highest activity towards the ORR (E_{onset} = 0.85 V vs. RHE). The presence of iron-based nanoparticles unaltered this activity, however, the presence of iron carbides encapsulated in the graphitic layer induces a change in the reaction mechanism as it was detected by hydrogen peroxide production. Based on the structure and catalytic activity results, we explore by DFT calculations the optimal distribution of the different N-moieties to increase the catalytic activity of Fe–N–C materials.

Experimental Section

Synthetic methods

Synthesis of Fe₃O₄ nanoparticles (NP). Fe₃O₄ nanoparticles were electrosynthesized using a modified electrochemical method reported by Herrasti et al.^[47] The general procedure consists in immersing two Fe electrodes (1 cm² for the anode and 2 cm² for the cathode, Fe sheets, 99.5% purity, 0.2 mm thick, purchased from Goodfellow) in a 0.04 M solution of sodium dodecyl sulfate as capping agent (Merck, ACS reagent, $\geq 99.0\%$) and 0.25 M sodium chloride (Sigma-Aldrich, ACS reagent, $\geq 99.0\%$), at room-temperature under magnetic stirring. A continuous DC of 100 mA cm^{−2} is

supplied for 30 minutes by a power source (BAKU, BK-305D 30V 5A). Then, the as-synthesized Fe_3O_4 nanoparticles were magnetically separated and successively washed with mili-Q water using an ultrasonic bath to remove the excess of the surfactant. The nanoparticles were kept in mili-Q water prior to be used. The electrode iron sheets were polished and washed with ethanol and mili-Q water to remove organic and inorganic surface residues before being used.

Synthesis of the catalysts

To evaluate the role of Fe_3O_4 nanoparticles as template and iron source in the activity of Fe–N–C pyrolyzed materials, two catalysts were synthesized using Fe_3O_4 nanoparticles as template, PANI as C–N source and FeCl_3 as iron source (Fe–PANI–NP and Fe–PANI@NP), and three different control catalysts (PANI, Fe–PANI, NP–PANI).

PANI: The polyaniline (PANI) sample was prepared according to an oxidative polymerization method reported in the literature.^[48] Aniline (Sigma-Aldrich, ACS reagent >99.5%) and ammonium peroxydisulfate (APS, Sigma-Aldrich, ACS reagent $\geq 98.0\%$) were mixed in a 0.1 M HCl solution under continuous stirring for 12 hours, keeping the temperature in a range of 0–5 °C. After completing the polymerization, the product was filtered and dried in an oven at 60 °C for 12 hours. The precursor's aniline:APS molar ratio was 1:1.

Fe–PANI: An FeCl_3 solution was dropwise added into an acidic solution of aniline (0.1 M HCl) and magnetic stirring at a temperature range of 0–5 °C (molar ratio 2.4:1 FeCl_3 :aniline). The oxidizing agent APS was added into the mixture with an APS to aniline molar ratio of 1:1. The mixture was stirred for 12 hours. Finally, the product was filtered and dried under a vacuum oven at 60 °C for 12 hours before the pyrolysis treatment.

NP–PANI: The previously synthesized nanoparticles were dispersed in water under ultrasonic conditions. The dispersion was added to acidic aniline solution (0.1 M HCl) under stirred conditions for 5 minutes. The oxidizing agent APS was dropwise added into the dispersion, and the mixture was stirred for 12 hours. The product was filtered and dried in a vacuum oven at 60 °C for 12 hours. The NP to aniline weight ratio was 1:2, and the APS to aniline molar ratio was 1:1.

Fe–PANI–NP: The synthesis is the same as in NP–PANI, but before adding the aniline precursor, anhydrous FeCl_3 (Sigma-Aldrich, 99.99%) was added to the dispersion under magnetic stirring for 30 minutes. The Fe^{3+} to aniline molar ratio was 2.4:1, and the NP to aniline weight ratio was 1:2. The product was filtered and dried in a vacuum oven at 60 °C for 12 hours before the heat treatment.

Fe–PANI@NP: The catalyst was synthesized following the previously reported procedure.^[49] The nanoparticles were dispersed in a 0.1 M HCl solution under sonication for 5 minutes. Then, the aniline precursor was added slowly from an acid solution into the dispersion under magnetic stirring, keeping the temperature in a range of 0–5 °C for 1 hour. The oxidizing agents APS and FeCl_3 were dropwise added into the dispersion, and the mixture was stirred for 12 hours. The product was filtered and dried in a vacuum oven at 60 °C for 12 hours. The NP to aniline weight ratio was 1:2, and the APS to aniline molar ratio was 1:1.

All the synthesized precursors were subjected to a first pyrolysis treatment at 1000 °C under an inert atmosphere (N_2) for 2 hours. The samples were leached with 0.5 M H_2SO_4 at 80 °C for 15 hours to remove all the metal ions and the uncoated nanoparticles. Finally, the composites were subjected to a second heat-treatment at

1000 °C under NH_3 atmosphere ($\text{NH}_3:\text{N}_2$ at 5%) for 30 more minutes.

Structural Characterization

Mössbauer spectroscopy details

The different iron species present in the catalysts were characterized by Mössbauer spectroscopy. The spectra were recorded at room temperature in triangular mode using a conventional spectrometer with a 50-mCi ^{57}Co (Rh) source. The spectral analyses were performed using the nonlinear adjustment fit of the NORMOS program.^[50] The calibration energy was calculated with an $\alpha\text{-Fe}$ (6 μm) foil spectrum, and the Isomer Shifts were referred to $\alpha\text{-Fe}$. The Fe proportions of each identified iron species within the catalysts were done assuming that the resonance probability is the same in all cases.

XPS spectroscopy details

XPS data were recorded with a PHOIBOS-150 electron analyzer (SPECS) under a pressure lower than $2 \cdot 10^{-9}$ mbar using Al K_{α} radiation and a constant pass energy of 20 eV. The binding energy scale was referenced to the main C–C 1s signal at 284.6 eV.

Morphological characterization

FE-SEM and TEM analysis: A Field Emission Scanning Electron Microscope (FESEM) of QUANTATM 250 FEG, Thermo Fisher Scientific, and a Transmission Electron Microscopy (TEM) performed on a JEM-1400Flash Electron Microscope at an acceleration voltage of 120 kV, were used to determine the shape and size distribution of the synthesized precursors and catalysts.

BET Surface determination

The surface area and porosity were determined through nitrogen adsorption/desorption isotherms, using the Brunauer-Emmett-Teller (BET) method at 77 K with a 3 Flex Micromeritics equipment. The obtaining of the micropores volume was carried out using the Barrette-Joynere-Halenda (BJH) method.

Electrochemical characterization

Preparation of powder inks and electrode modification

Glassy carbon (GC) electrodes were modified using powder inks prepared from the five synthesized catalysts as follows: 0.001 g of each catalyst were dispersed in 4 mL of isopropanol and 1 mL of Milli-Q water solution. The mixtures were ultrasonicated for 30 min until form a homogenous dispersion. Then, Nafion (20 μL , 5 wt% in alcohols, Sigma-Aldrich) was added to the mixture and sonicated for 10 more minutes. The GC electrodes were modified with 10 μL of each ink and dried under a nitrogen flow.

Electrochemical measurements

The electrochemical experiments were performed with a bipotentiostat (CH Instruments, CH1720E) in a conventional electrochemical cell with a rotating ring-disk electrode as the working electrode, and a graphite rod and a saturated calomel electrode (SCE_{sat}) as the counter and reference electrodes, respectively. The electrochemical characterization was performed by cyclic voltammetry (CV) under a

N_2 atmosphere in acid (0.1 M $HClO_4$) at 5 mVs^{-1} . To study the catalytic activity towards the ORR, polarization curves were performed in the respective acid oxygen saturated electrolytes at 25°C , varying the rotation rate and holding the Pt ring of the RRDE at a potential where the hydrogen peroxide detection is limited by diffusional regime ($V = 1.2\text{ V vs. RHE}$).^[51] Additionally, the role of iron centers in the catalysis was studied by an alkaline CN^- poisoning test in O_2 -saturated 0.1 M NaOH basic media with a 10 mM KCN. All the potential are referred to RHE scale, $E_{(RHE)} = E_{app(SCE)} + 0.242 + 0.059 \cdot pH$, (E_{app} = applied potential).

Computational details

Density Functional Theory (DFT) calculations were performed to study the electronic structure and $Fe-O_2$ adsorption energy of the $Fe^{II}N_4C_{10}$ models (*clean* and N-substituted). The geometry optimizations were done using Gaussian 16 software.^[52] All the calculations were performed at the PBE0/TZVP^[53,54] level, including the DFT-D3 dispersion force corrections for self-consistent field energies.^[55] For the electronic distribution analyses, the Hirshfeld atomic charges^[56] were considered. The optimized geometries at the global minimum in energy were confirmed by vibrational analysis.

Results and Discussion

Structural Characterization

The final morphology of the pyrolyzed materials was characterized by FE-SEM and TEM. FE-SEM images obtained for non-pyrolyzed precursors NP and NP-PANI (Figures S1a and b, respectively) showed a diameter size distribution of c.a. 40 nm. Figure S1b shows that the NPs are covered with PANI. In addition, Figures S1c and d show the representative TEM images of Fe-PANI-NP and Fe-PANI@NP catalysts after the second pyrolysis process, respectively. The catalysts present a heterogeneous graphitized carbon structure with different shapes and dimensions and iron nanoparticles covered by graphitic layers. However, the structure of the NPs seems to be different in each catalyst, while in Fe-PANI-NP the particles present a non-uniform size covered by an irregular carbon-based graphitic layer, in Fe-PANI@NP catalysts, the NPs are regular with a similar carbon graphitized thickness.

The surface area of the different catalysts was studied using N_2 adsorption-desorption isotherms. The values of the surface areas and average pore diameter are presented in Table S1. As can be observed the use of NP as template increases the surface area from $\sim 400\text{ m}^2\text{ g}^{-1}$ to $1000\text{ m}^2\text{ g}^{-1}$.

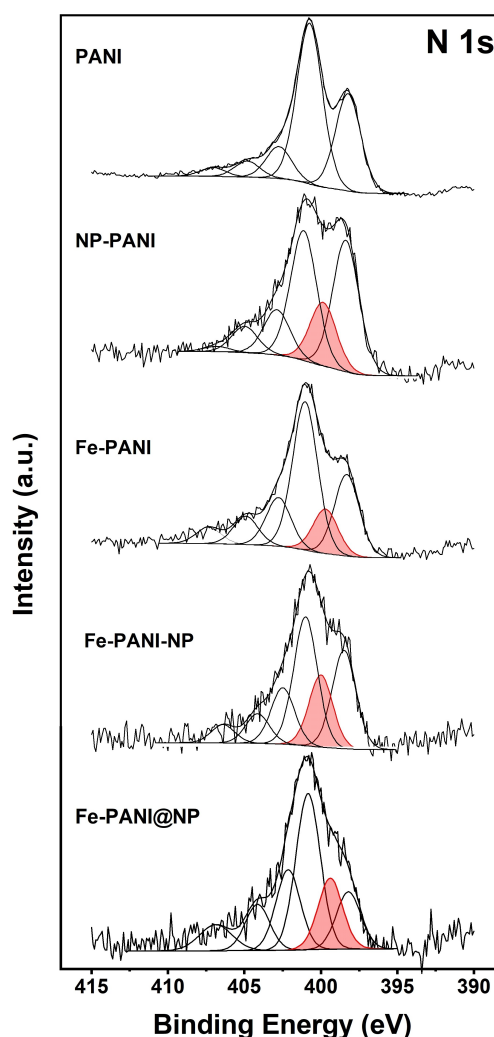


Figure 1. XPS N1s spectra recorded from (a) PANI, (b) NP-PANI, (c) Fe-PANI, (d) Fe-PANI-NP and (e) Fe-PANI@NP. Red area represents the contribution of Nx-Fe.

The surface characterization of the N-containing functionalities was performed by XPS. Figure 1 shows the N1s XPS spectra recorded from synthesized catalysts: PANI, NP-PANI, Fe-PANI, Fe-PANI-NP and Fe-PANI@NP. The spectra recorded were fitted to six contributions, all having the same linewidth. Table 1 collects the relative atomic concentrations for each nitrogen species obtained from the fit of the XPS data. The assignment was done according to previously reported literature.^[11,16] As can be observed in Table 1, the pyrolysis of PANI (without iron

Table 1. Relative areas (%) of the N-contributions obtained from the fit of the N1s XPS spectra for the different catalysts.

Catalysts	N-pyridinic 398.2 eV	Nx-Fe 399.8 eV	N-pyrrolic 400.8 eV	N-graphitic 402.9 eV	N-oxides 404.4 eV	N-oxides 407.0 eV
PANI	31	–	51	10	5	3
NP-PANI	33	16	32	11	7	1
Fe-PANI	22	12	40	13	8	5
Fe-PANI-NP	24	18	32	14	7	5
Fe-PANI@NP	13	16	35	18	10	8

source) induces the formation of a high quantity of superficial N-pyridinic and N-pyrrolic functions with a lower amount of N-graphitic and oxidized N sites. The presence of iron salts and/or Fe₃O₄ nanoparticles in the synthetic route induces the development of Nx-Fe species in the catalysts having different proportions from sample to sample: NP-PANI, Fe-PANI-NP, and Fe-PANI@NP catalysts showed higher relative area values (%) than the Fe-PANI catalyst. As can be observed in Table 1, the combination of NP and FeCl₃ reduce the presence of N-pyridinic and increase the presence of N-graphitic species in the final catalysts. However, there is not a clear trend in the Nx-Fe actives sites since their relative areas remain constant in the catalysts, except in the case of Fe-PANI where the amount of Nx-Fe decreases by a significant amount. The signals above 402.9 eV, associated with N-oxides with different bond multiplicities (evidenced by two different signals) show a similar contribution in all the samples.

The role of Fe₃O₄ nanoparticles during the synthesis was studied by Mössbauer spectroscopy after the first and the second pyrolysis processes in NP-PANI catalysts. Figure 2a shows the spectrum recorded after the first pyrolysis process (900 °C, N₂ atmosphere, named NP-PANI(N₂)), and Figure 2b shows the spectrum after the acid leaching and the second pyrolysis process (950 °C, NH₃ atmosphere, named NP-PANI(NH₃)). The assignment of the different iron species was made based on previous studies,^[57] and the structural parameters are summarized in Table S2. The full widths at half maximum (FWHM) of some subspectra and the 3:2:1:1:1:2:3 intensity ratio for the sextets were fixed in the spectra fitting. The spectrum recorded after the first pyrolysis was deconvoluted into four different iron contributions corresponding to different iron-based particles and moieties developed during the pyrolysis. The assigned signals as four sextets are contributions due to α -Fe particles, Fe-carbide particles (Fe₃C), and Fe₃O₄ particles (characterized by two sextets), respectively.^[58,59] The fourth signal assigned as a doublet (D1) was attributed to the presence of low-spin iron-nitrogen sites Fe²⁺N₄/C (S=0) inserted in the carbonaceous material.^[19,59–61] As shown in Figure 2b, the spectrum changes after the acid leaching and the second pyrolysis process, there is a lack of the sextets

associated to Fe₃O₄ due to the acid treatment that dissolves the uncovered Fe₃O₄ particles.^[15,23,29,62] In the spectrum appears a new singlet associated with antiferromagnetic iron γ -Fe fcc particles typically formed above 917 °C and later quenching.^[63] The development and stabilization of these allotropic iron species are due to the graphitization of the carbon matrix that kinetically hinders its thermodynamically favored conversion to α -Fe.^[63] The above is corroborated by the decrease of the α -Fe species content ($\Delta[\% \alpha\text{-Fe}(\text{NP-PANI-NH}_3) - \% \alpha\text{-Fe}(\text{NP-PANI-N}_2)] = -26\%$ relative % area). In addition, the carbide particles (Fe₃C) content increases, being the major species with a relative area of 47%, which agrees with the decomposition of Fe₃O₄^[29] and FeN₄ species detected in Fe-PANI(N₂). The minority contribution of D1 after the second pyrolysis process is attributed to the acid washing that can also decompose part of the FeN₄/C sites. Noteworthy, in both NP-PANI catalysts synthesized only with magnetite NPs as precursor (without iron salt), only low-spin FeN₄ species (D1) were detected in the carbon graphitized matrices.

Figure 3 shows the Mössbauer spectra recorded from the catalysts Fe-PANI, Fe-PANI-NP, and Fe-PANI@NP, after the second pyrolysis process under NH₃. The spectra of Fe-PANI and Fe-PANI-NP catalysts (Figure 3a, 3b) were deconvoluted using the same subspectra as in the previous case: two sextets for α -Fe and FeC₃, one singlet for γ -Fe fcc, and two doublets assigned to Fe²⁺N₄/C sites (S=1 and S=0). The sextets and the singlet have the same assignment as the NP-PANI(NH₃) case (Figure 2b). However, instead of only one doublet corresponding to Fe²⁺N₄/C sites (S=0), a new doublet appears, which is assigned to a medium spin (S=1) Fe²⁺N₄/C, having a geometry similar to that found in iron-phthalocyanines complexes (FeN₄, S=1; with IS near to 0.3 mm/s and EQ near to 2.6 mm/s.^[19,59,60,64–66] The differentiation between D1 and D2 is based on their quadrupole splitting values, which shift to higher values for D2 (D1, EQ = 0.9 mm s⁻¹ and D2, EQ = 2.6 mm s⁻¹). This differentiation is related to the iron center's loss of symmetry in the Fe²⁺N₄/C unit.^[16,20,21,66,67] The presence of D1 and D2 contributions in both Mössbauer spectra is interesting since both catalysts were synthesized with iron salt as precursor (FeCl₃) (and without magnetite NPs Fe-PANI), which indicates that the use of Fe₃O₄

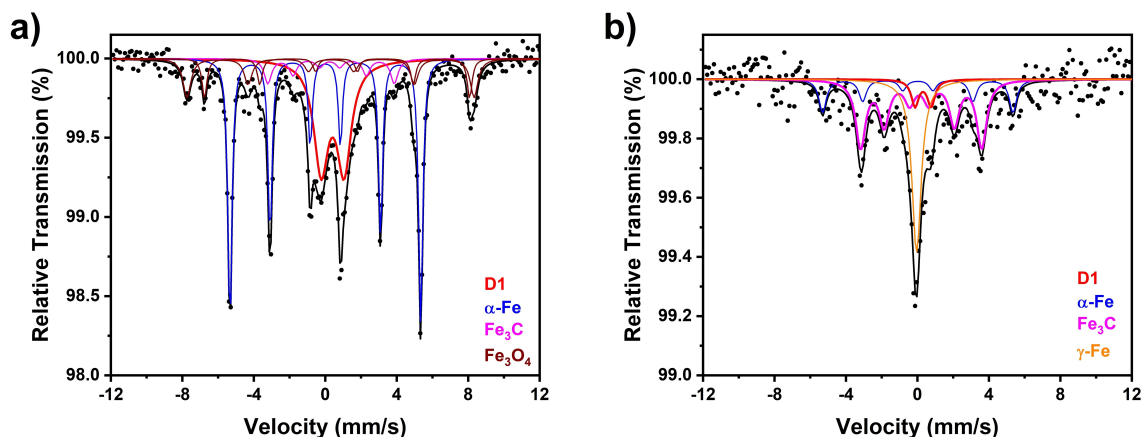


Figure 2. Mössbauer spectra recorded from (a) NP-PANI (N₂), and (b) NP-PANI (NH₃).

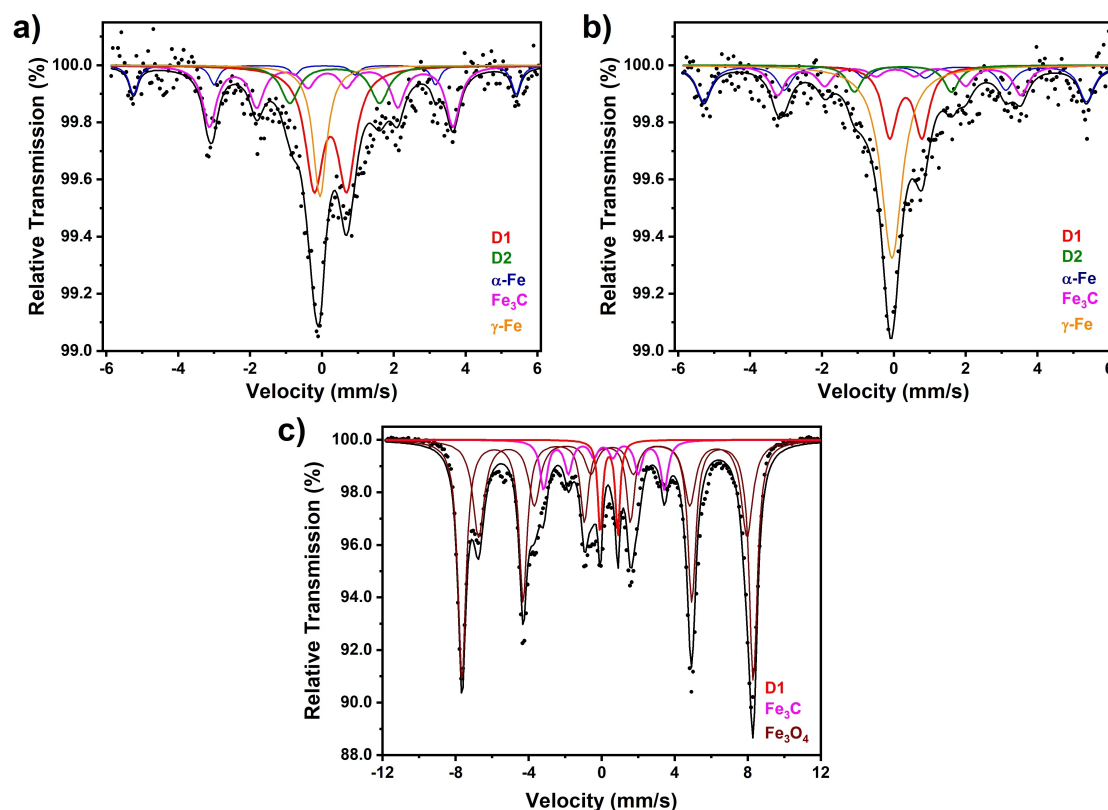


Figure 3. Mössbauer spectra recorded from (a) Fe-PANI, (b) Fe-PANI-NP ($v \sim 6 \text{ mm s}^{-1}$) and (c) Fe-PANI@NP ($v \sim 12 \text{ mm s}^{-1}$). Spectra for Fe-PANI and Fe-PANI-NP were also measured with $v \sim 12 \text{ mm s}^{-1}$ to discard the presence of magnetite NPs.

NPs as precursor promotes the formation of D1 sites over D2. In addition, the quantitative dominance of the metallic iron particles (α -, γ -Fe, and Fe_3C) embedded and covered by the carbon graphitic layer suggests their high inclusion over the Fe–N–C matrices as anchored components. Figure 3c shows the Mössbauer spectrum recorded from the Fe-PANI@NP catalyst, which was best fitted to one doublet ($\text{Fe}^{2+}\text{N}_4/\text{C}$ ($S=0$)), one sextet (FeC_3), and two sextets (Fe_3O_4). The presence of Fe_3O_4 NP confirms the successful polymer coating of the nanoparticles, which prevents their dissolution during the acid treatment and subsequent pyrolysis (as can be appreciated in the FESEM morphological characterization shown in Figure S1b). In addition, the development of other iron particles as α -, γ -Fe seems to be hindered by the synthetic route and the proportion of Fe_3C in the final catalyst.

Electrochemical characterization and electrocatalytic analysis

The electrochemical characterizations of the different materials were performed by cyclic voltammetry in N_2 saturated acid media. The voltammograms are presented in Figure 4, and the electrochemical parameters are summarized in Table 2. The voltammogram recorded from the PANI catalyst presents a capacitive behavior characteristic of N-doped carbon materials.^[68] However, the presence of an iron source in the synthetic route, either as Fe_3O_4 or FeCl_3 , induces the presence of different faradaic processes in the catalysts. The signal recorded from NP-PANI shows a clear faradic peak close to 0.5 V vs. RHE, which is associated with the Fe(III)/Fe(II) redox process of the Fe–N4 sites inserted in the carbon graphitized matrices, which are detected by both XPS and Mössbauer spectroscopies. These FeN4 units are developed during the pyrolysis process where the superficial iron of the Fe_3O_4 nanoparticles acts as iron

Table 2. Electrochemical parameters for the synthesized catalysts.

Sample	$E_{\text{red}}/[\text{V vs.}] \text{ RHE}$	$E_{\text{on-set}}/[\text{V vs.}] \text{ RHE}$	Tafel slope/ V dec^{-1}		n° electrons Disk-Ring
			Low overpotentials	High overpotentials	
PANI	–	0.449 ± 0.001	–	0.173 ± 0.001	3.6 ± 0.1
NP-PANI	0.592 ± 0.006	0.622 ± 0.001	0.126 ± 0.004	0.205 ± 0.002	3.8 ± 0.1
Fe-PANI	0.70 ± 0.03	0.705 ± 0.001	0.069 ± 0.005	0.129 ± 0.002	3.8 ± 0.1
Fe-PANI-NP	0.720 ± 0.004	0.848 ± 0.002	0.071 ± 0.003	0.125 ± 0.002	3.7 ± 0.1
Fe-PANI@NP	0.726 ± 0.005	0.852 ± 0.001	0.067 ± 0.001	0.121 ± 0.001	3.9 ± 0.1

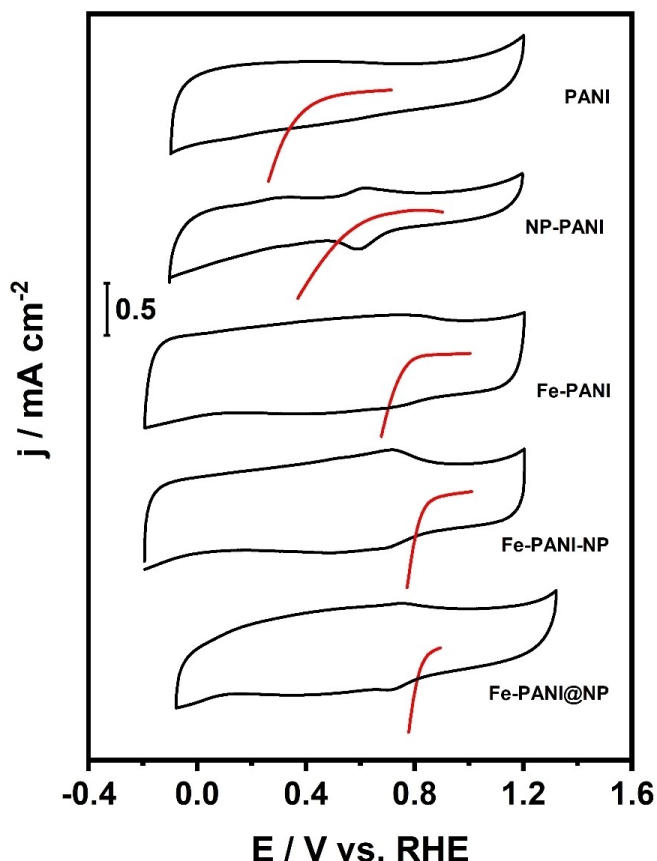


Figure 4. Electrochemical characterization by cyclic voltammetry of the catalysts in N_2 saturated acid media H_2SO_4 0.1 M (black line) and kinetic currents at 1600 r.p.m, scan rate 0.005 Vs^{-1} for ORR (red lines) in O_2 saturated acid media.

sources at high temperatures. However, the presence of FeN4 active centers has not been described previously when iron nanoparticles are used as templates.^[29] In the voltammogram of the catalysts synthesized without NP but with Fe^{3+} , Fe-PANI, the signal recorded presents the same Fe(III)/Fe(II) faradaic process but shifted 100 mV to more positive values (see Table 2). The two catalysts synthesized using NP as template and Fe^{3+} as an iron source ($FeCl_3$) present a similar voltammogram with a clear redox process for both materials at similar potential values (0.720 V and 0.726 V vs RHE, respectively). The presence of a Fe(III)/Fe(II) redox process corroborates the chemical and structural characterization of the catalyst carried out by XPS (N 1s spectra, Figure 1 and Table 1), and Mössbauer spectroscopy (presence of quadrupole doublets, Figure 3b and 3c). A remarkable fact is the different potential values for the Fe(III)/Fe(II) process, which is most likely related to the chemical environment of the active centers since the electron-withdrawing or electron-donating nature of the N-doped species and defects generated during the pyrolysis process modify the electronic structure of the Fe atoms of the FeN4 moieties.

To reveal the influence of the electronic structure of the iron active centers with the electrocatalytic activity, the kinetic current of the polarizations curves (extracted from Figure 5a) is presented in Figure 4 (red lines). As can be observed, the onset

potentials for the ORR are connected with the aforementioned redox process Fe(III)/Fe(II), which implies that the Fe(II) species electrogenerated during the cathodic polarization acts as active sites for the ORR. In addition, this connection corroborates that the redox potential of the catalysts ($E^{o'}_{(Fe(III)/Fe(II))}$) is a well-known ORR reactivity descriptor for the pyrolyzed Fe–N–C materials, as well as for other MN4 molecular complexes such as metalloporphyrins and metallophthalocyanines.^[41,69,70]

The electrocatalytic activities of the different synthesized materials were measured with a RRDE in O_2 saturated acid media. Figure 5a shows the polarization curves registered for the ORR and the current detected at the platinum-ring electrode for the hydrogen peroxide generated at 1600 r.p.m. As can be observed in Figure 5a, the catalysts synthesized using Fe_3O_4 NPs and Fe^{3+} as iron source present the highest onset potential ($E_{onset}=0.82\text{ V vs. RHE}$), followed by the catalysts synthesized only with Fe^{3+} but without NP. The catalysts PANI and PANI-NP present lower onset potential values towards the ORR. Considering that the catalysts synthesized with an iron source (NP, $FeCl_3$, or both) present FeN4 active sites, the difference in the onset potentials reveals the importance of the electronic density of the active sites for the electrocatalysis. The selectivity of the reaction for the total or partial reduction of O_2 to H_2O or H_2O_2 , respectively, was studied by the determination of the number of electrons from the ring currents collected and presented in Figure 5a. For all the catalysts, the number of electrons calculated (eq. S1) was higher than 3.5, which informs on the high selectivity of these materials for the total reduction to H_2O . However, there are differences in this selectivity according to the applied potential. Figure 5b shows the evolution of the electrons transferred during the polarization experiments. As can be noted in Figure 5b, the catalyst Fe-PANI@NP present a total reduction to H_2O from the onset potential; however, for the catalyst Fe-PANI-NP this selectivity to 4e⁻ increases with the applied potential. Instead of the number of electrons, the percentage of H_2O_2 generated during the polarization tests informs the reaction mechanism.

There is a consensus that for molecular and pyrolyzed catalysts an H_2O_2 yield lower than c.a. 20 % the O_2 is reduced via a direct 4-electrons pathway, whilst for a higher yield, the mechanism is related to a 2×2 electron transfer mechanism.^[34,70–72] Due to the different catalytic active sites present in pyrolyzed catalysts, the catalytic activity of the active sites and the mechanism is potential dependent.^[70] At low overpotentials, the FeN4 active sites are the responsible for the electrocatalytic activity (close to the onset potential). In contrast, at high overpotentials, the secondary N-sites might become active for the catalytic process, and they could modify the mechanism acting as primary and secondary active sites. This implies that the samples with similar onset potential and amount of active sites (FeN4) the catalysts Fe-PANI-NP and Fe-PANI@NP present a different overall mechanism for the total reduction of O_2 to H_2O_2 , being the adsorption of H_2O_2 on the iron active centers a key parameter for the mechanism via 4 or 2×2e⁻ pathway.

The study of the *r.d.s* and the mechanism for the ORR was made based on the Tafel slopes determined from the kinetic

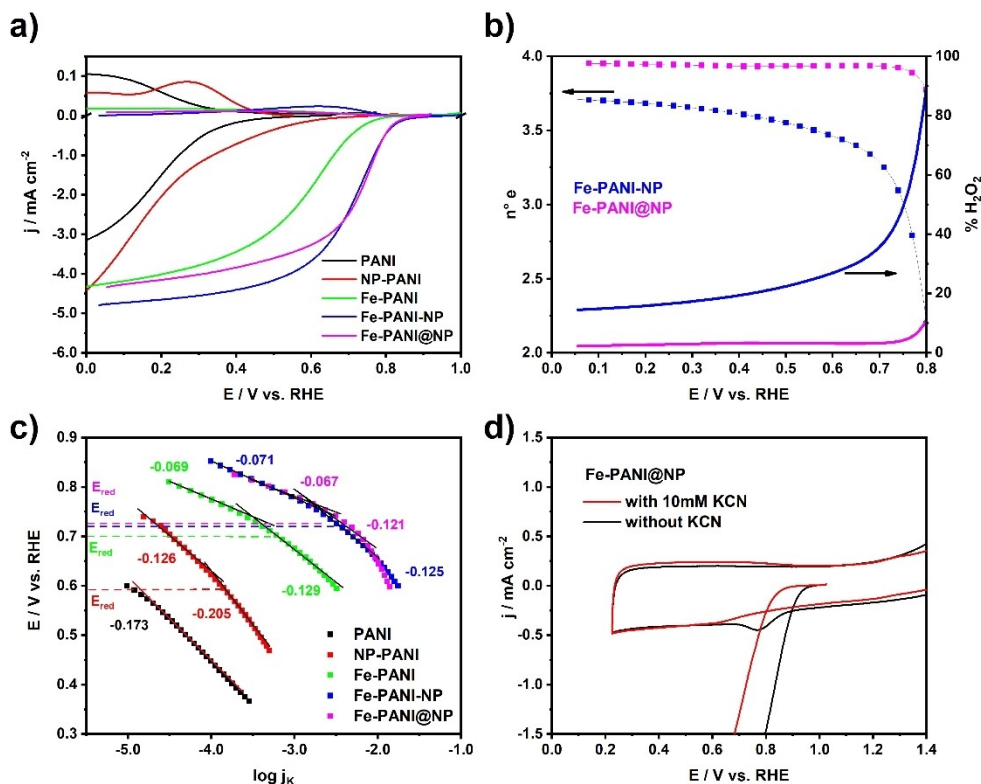
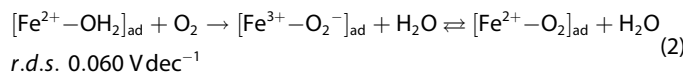
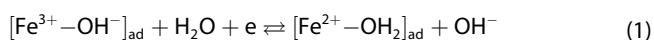


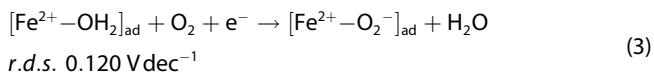
Figure 5. (a) Polarization curves in acid media at 1600 r.p.m, scan rate 0.005 V s⁻¹ for O₂ reduction. (b) Percentage of peroxide and electrons transferred in the ORR for Fe-PANI-NP and Fe-PANI@NP. (c) Tafel slopes for pyrolyzed catalysts at low and high overpotentials. (d) Cyclic voltammetry of Fe-PANI@NP with (red line) and without (black line) 10 mM KCN in N₂ saturated 0.1 M NaOH, scan rate 0.050 V s⁻¹, including the linear sweep voltammetry measured in O₂ saturated 0.1 M NaOH, 1600 r.p.m. and scan rate of 0.005 V s⁻¹.

part of the polarization curves, previously corrected by mass transport $j_k = [(j_L - j)/(j_L - j_0)]^{1/2}$.^[51] Figure 5c shows the Tafel plots for the catalysts. There is a common trend in the iron-containing catalysts: the presence of two slopes that change the values close to the Fe(III)/Fe(II) redox potential determined by cyclic voltammetry. The Tafel slope values change from c.a. 0.060 to c.a. 0.12 V dec⁻¹, implying that the Fe(II) electrogenerated is the active site for the ORR and an inner-sphere mechanism, as it has been reported previously for Fe-N-C catalyst in acid media.^[70,73] According to the Tafel slopes and the connection between the onset potential with the redox potential Fe(III)/Fe(II), the mechanism of ORR on these materials can be described as follows:

At low overpotentials:



At high overpotentials:



At low overpotential, the amount of Fe(II) is potential-dependent and can be estimated through the Nernst equation for adsorbed species assuming an ideal behavior and an applied potential greater than Fe(II)/Fe(I).^[70]

$$\theta(\text{Fe(II)}) = \frac{1}{1 + \exp \left(\frac{F(E - E_{\text{Fe(III)/Fe(II)}}^0)}{RT} \right)} \quad (4)$$

Based on this, the rate equation for low overpotential can be expressed as the current density dependent on the applied potential and the energy of O₂ adsorption, described by the following kinetic equation:

$$i = nFk(1 - \theta)(p\text{O}_2) \Gamma \left(\exp - \beta \Delta G_{\text{ad}}^0 / RT \right) \exp \left(- \left(\frac{F}{RT} E - E_{\text{Fe(III)/Fe(II)}}^0 \right) \right) \quad (5)$$

At higher overpotentials with slopes of -0.120 mV dec⁻¹, when $E_{\text{Fe(III)/Fe(II)}}^0 > E > E_{\text{Fe(II)/Fe(I)}}^0$ the Fe(II) occupied sites are at maximum ($\theta_{\text{Fe(II)}} = 1$). Therefore, the kinetic equation is dependent on O₂ adsorption and the electron transfer at the applied potential:

$$i = nFk\Gamma(1 - \theta)(p\text{O}_2) \exp(-\beta \Delta G_{\text{ad}}^0 / RT) \exp(-\alpha nF(E - E_{\text{eq}}) / RT) \quad (6)$$

As described in eq. 5 and 6, the redox behavior of the metal center has an important role in the catalytic process. To corroborate the iron implication as active site, a poisoning test was carried out in basic- O_2 saturated media with the presence of CN^- , which has a strong interaction with $Fe(III)$.^[74] The polarization curves and the cyclic voltammograms for Fe-PANI@NP in poisoning tests are presented in Figure 5d, in which the ORR activity decreases in the presence of CN^- which corroborates that the $Fe(II)$ is the active site for the ORR. In addition, the cathodic redox process $Fe(III)/Fe(II)$ is hindered, as can be observed in the CV tests.

In order to link the catalyst characterization with the catalytic activity, the efforts were focused on finding activity-structural relations as reactivity descriptors to explain the catalytic activity and mechanism differences on the basis of their composition. Among the different reactivity descriptors presented in the literature,^[35,75] the redox potential $Fe(III)/Fe(II)$ of the metal center determined by cyclic voltammetry presents a good linear correlation with the activity expressed as the current density at a constant potential. Figure 6a presents this linear correlation where catalysts previously reported have also been included (gray squares). As can be observed, the catalytic activity increases when the redox potential does, corroborating that the redox potential of the metal center is a good reactivity descriptor for the ORR with Fe–N–C catalysts.^[57,69] Based on the

link between the redox potential and the catalytic activity, the catalysts activity seems to be related to the electronic density of the metal iron center and not to the amount of active sites in the catalysts (see Table 1). To elucidate the influence of the N-functionalities present in the graphitic carbon layer on the electronic density of metal center, the amount of N_{pyr} and N_{graph} determined by XPS is represented versus the redox potential of the catalyst in Figure 6b. As can be observed, the redox potential shift towards more positive values (lower electronic density) when the amount of N-graphitic content increases, and the opposite relation is found for the N-pyridinic content, where the redox potential decreases when the N content increases.

The influence of the N-functions content (pyridinic and graphitic) on pyrolyzed Fe–N–C catalysts' ORR activity has been widely studied in the literature.^[14,33–35] N-pyridinic/graphitic functions exhibit soft or intermediary character and can act as π -acceptor ligands, modifying the electronic density of neighboring atoms as carbon in a graphitized matrix^[37–40] or metal centers as iron in the same way as electron-withdrawing substituents in MN4 non pyrolyzed and pyrolyzed macrocycles.^[21,41] To include both N functionalities, Figure 6c presents the redox potential variation with the $N_{pyr}:N_{graph}$ ratio. As can be observed, when this ratio decreases, the catalyst's redox potential increases and hence the catalytic activity for the ORR.

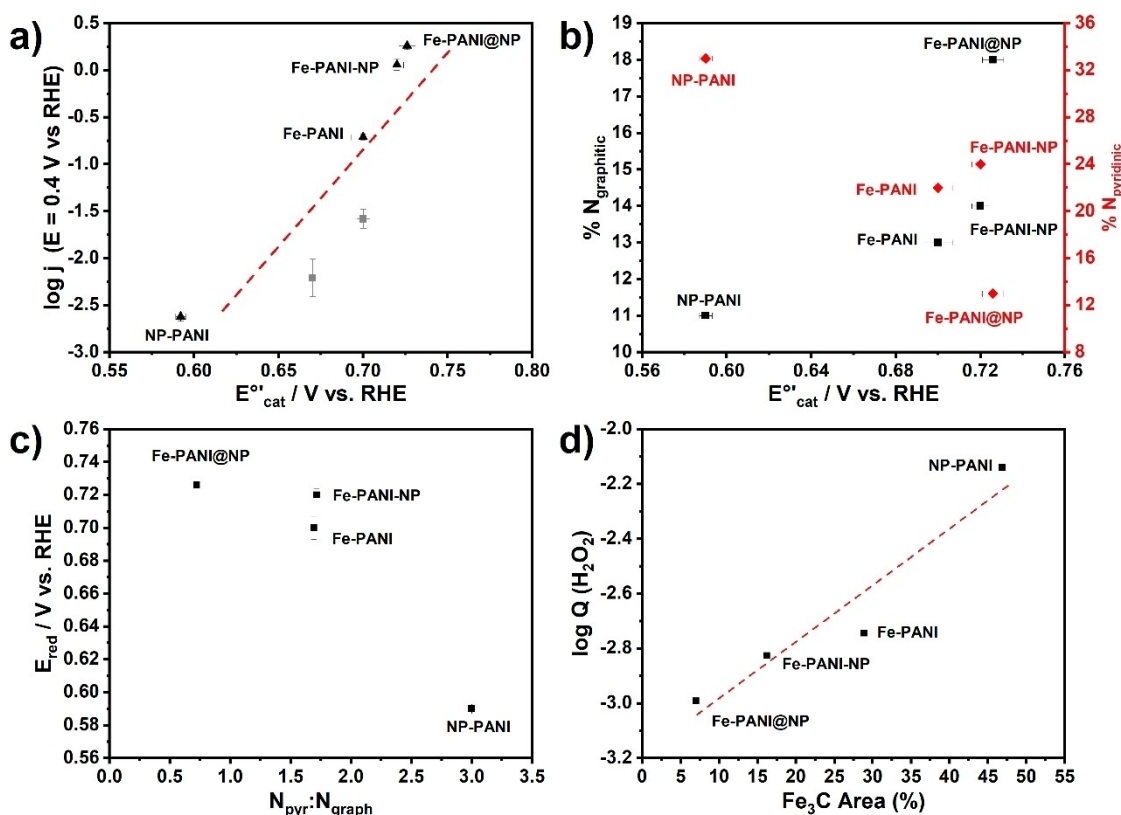


Figure 6. (a) Correlation of the activity represented as $\log j_k$ versus the $Fe(III)/Fe(II)$ formal potential of catalysts presented in this work (black symbols) and heat-treated MN4 catalysts (grey symbols).^[73] (b) Correlation between $Fe(III)/Fe(II)$ formal potential (E_{cat}^0) in function of the N_{graph} and N_{pyr} content determined by N1s XPS. (c) The E_{cat}^0 represented in function of $N_{pyr}:N_{graph}$ ratio. The $N_{pyr}:N_{graph}$ ratio was calculated with the % relative to total N content determined by N1s XPS. (d) Amount of hydrogen peroxide produced during the ORR represented as $\log Q$ normalized by the electrode surface area calculated from the integration of the area under the ring current curves vs. the Fe_3C amount determined by Mössbauer spectroscopy.

In addition, the selectivity of the catalysts for the ORR via a direct $4e^-$ or $2 \times 2e^-$ has been evaluated considering the secondary iron-based particles covered by the graphitic carbon layer identified by Mössbauer spectroscopy, and more specifically, on the amount of Fe_3C particles identified in each catalyst. Figure 6d shows the amount of hydrogen peroxide determined integrating the area of the ring current curves for each catalyst versus the amount of Fe_3C particles quantified by Mössbauer spectroscopy. It can be observed that there is a linear relationship between both parameters, showing that the presence of Fe_3C particles in the catalysts favors the H_2O_2 production. In addition, considering the aforementioned limit of 20 % to elucidate if the mechanism goes via direct $4e^-$ or $2 \times 2e^-$ pathways, the relation between the amount of Fe_3C and the mechanism is presented in Figure 6d. The role of these particles as secondary sites in promoting the $2 \times 2e^-$ mechanism has been previously confirmed, evidencing their capacity to electronically activate the covering carbon surfaces by lowering their local function work.^[29] Therefore, despite the lower influence of the Fe_3C in the catalytic activity in our catalysts, their presence seems to be critical for the production of H_2O_2 , which is detrimental for the long-term stability *in operando* conditions since the carbon matrix can be oxidized, inducing demetallation.^[42,57,76]

The spin and charge density redistribution caused by the inclusion of N-pyridinic functions^[38,40] has a special role in the selectivity of the reaction. The N_{pyr} functions have been identified as Lewis base sites, modifying the neighboring carbons^[36] turning them into secondary active sites where the adsorption of oxygen and its derivatives in acid media is favored.^[46] Hence, the presence of N_{pyr} promotes the creation of secondary active sites that can complete the reduction of H_2O_2 to H_2O .^[14] This fact can be extrapolated to Fe–N–C materials since the presence of N-functions directly influences the acidity of the Fe active sites, shifting the redox potential and acting as secondary active sites. Therefore, the $N_{pyr}:N_{graph}$ ratio can be useful to tune the selectivity of these catalysts for the ORR. At low overpotentials, the Fe(III)/Fe(II) redox process generates the Fe(II) active site for the ORR, and at high overpotentials, the secondary sites induced by the inclusion of N-functions (specially N_{pyr}) promotes the reduction of the hydrogen peroxide coming from a partial reduction of O_2 in the primary (Fe(II)) active center.^[34,70] This fact explains the percentage of H_2O_2 observed for Fe-PANI-NP at low overpotentials (over 20 %) and its decreases at higher overpotentials (Figure 5b) following a 2×2 mechanism. In this sense, Ning et al. demonstrated the importance of the synergism of N-pyridinic and N-graphitic sites in metal-free NG (N-doped graphene) catalysts for ORR through the correlation of the $N_{pyr}:N_{graph}$ ratio with the ORR activity in basic media, showing that with a $N_{pyr}:N_{graph}$ ratio near to 0.5 the activity is lowered, while for values above 0.5, the activity can be enhanced.^[77] Figure 6c shows the Fe(III)/(II) formal potential of the studied catalyst in function of their $N_{pyr}:N_{graph}$ ratio. The obtained trend for our catalysts is the opposite of that one reported by Ning et al. for metal-free NG catalysts, indicating that the ORR activity for Fe–N–C catalysts increases with a close N_{pyr} and N_{graph} surface content (ratio close to 0.5).

To corroborate the influence of N-pyridinic/graphitic functions on the catalytic activity of the active centers FeN4, the influence of the N-functionalities on the active centers was evaluated by DFT calculations. Fe^{II}N4C10 models with N_{graph} and N_{pyr} protonated functions inserted in different positions and distances to the iron centers (Fe/N) were evaluated, as can be observed in Figure 7a,b (see Computational Details). Fe^{II}N4C10 model was selected since it has been described in the literature as a possible structure motif in single-atomic FeN4 active sites inserted in graphitized Fe–N–C matrices.^[21,42,45,60,66] A $+2$ -oxidation state for the iron centers was selected and the low-spin configuration ($S=0$) of the Fe atom established for the models is in concordance with the assignment of D1-FeN4 units in our catalysts (according to Mössbauer spectroscopy characterization, Table S2). Noteworthy, the literature suggests that the orbital population availability of FeN4 units in the low-spin state ($S=0$) compared to that of middle- ($S=1$) or high-spin states ($S=2$) is expected to favor the interaction with O_2 molecules and therefore enhance the ORR activity.^[20] Figures 7c and 7d show the correlation between the iron(II) charges (Hirshfeld charge) for the *clean* (without any substitution) and the substituted models with N-functions at different Fe/N distances, where an evident variation of the Fe-charge with the distance is observed. For N_{graph} functions, the iron charge shifts to more positive values when the N_{graph} -FeN4 distance decreases, which implies that the acid character of the iron centers is higher at Fe/ N_{graph} distances < 5.5 Å. However, for N_{pyr} functionalities, the opposite effect is found, and the acid character of the iron center increases when the Fe/ N_{pyr} distance does (at Fe/ N_{pyr} distances > 6.5 Å).

In order to evaluate the increase of the acidity in the catalytic activity of the iron centers due to the interaction with the N-functionalities, the donor-acceptor chemical potential descriptor ($\Delta\mu_{A-D}$)^[78,79] was determined for each Fe/N distance and functionalities (Figure S2). This descriptor evaluates the catalytic activity for the ORR. An increase in the $\Delta\mu_{A-D}$ values implies an increase in the catalytic activity, considering the *clean* and the substituted models as the donor molecules (D) and the dioxygen molecule as the acceptor one (A). The results show an increase in the catalytic activity when any N-functionalities (N_{pyr} or N_{graph}) are inserted in the model, independently of the distance.

In addition, the N-functionalities also induce an electronic modification over the frontier molecular orbitals dz^2 and dxz of iron centers, depending on their nature and the nitrogen-to-metal distances Fe/N. Figures 8a and b show the variation of the energy of the dz^2 orbital according to the N_{pyr} or N_{graph} function and the Fe/N distance. As can be observed, the energy of the orbitals and hence their occupancy depends on the N-functionalities: for N_{graph} the unoccupancy of the orbitals take place at distances below 5.5 Å, while for N_{pyr} it occurs at a distance above to 6.5 Å. Moreover, coupled to the unfilled dz^2 orbital, the dxz orbitals get filled (Figure S3). The energy and unoccupancy of the iron dz^2 orbital determine the Fe– O_2 binding over the *xy* FeN4 plane,^[41,80–82] reflected by the calculated Fe– O_2 adsorption energy (E_{ad} , Figure 9a), a widely used ORR reactivity descriptor for MN4-type catalysts.^[69] The E_{ad}

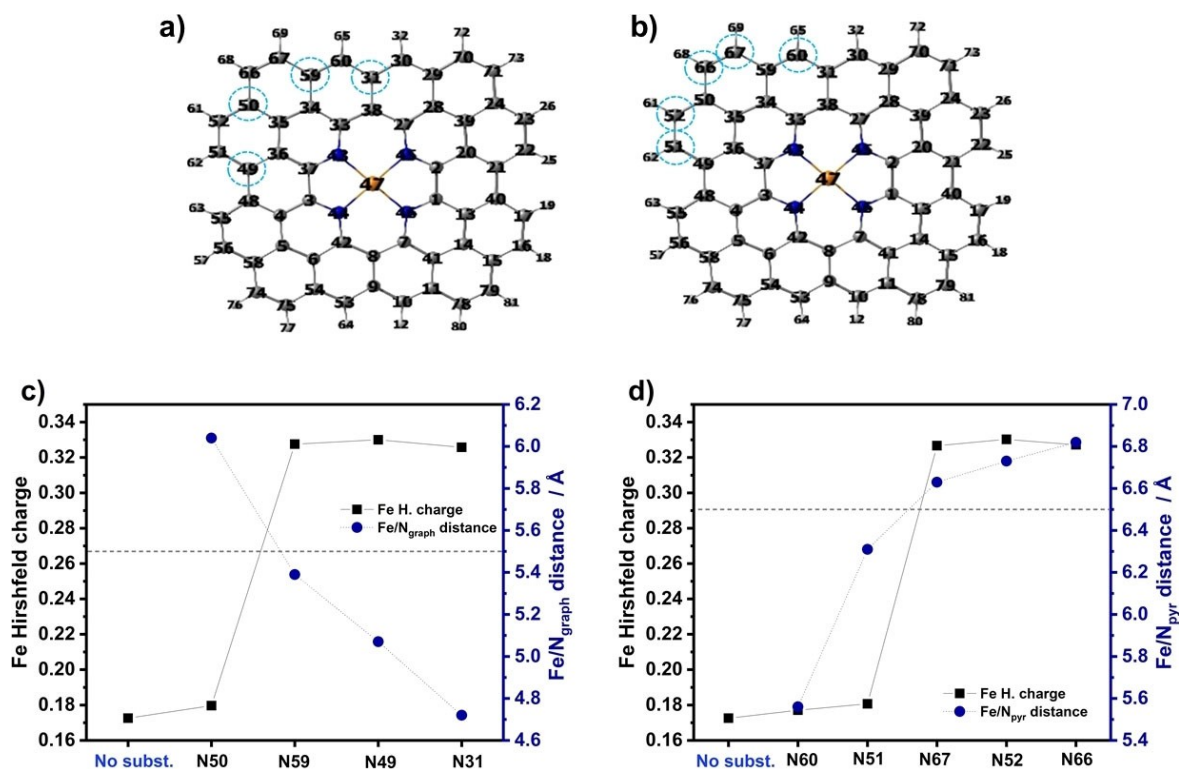


Figure 7. Ball and stick representation of the Fe^{II}N4C10 models, showing the added N substitutions: (a) N-graphitic (N_{graph}) and (b) N-pyridinic protonated (N_{pyr}) (grey = carbon, white = hydrogen, blue = nitrogen, orange = iron). Calculated Fe Hirshfeld charge for the optimized models (*clean* and substituted Fe^{II}N4C10 models) correlated with the N-function to FeN4 distance (Fe/N_{subst} distance) for (c) N_{graph} and (d) N_{pyr} Fe^{II}N4C10 models.

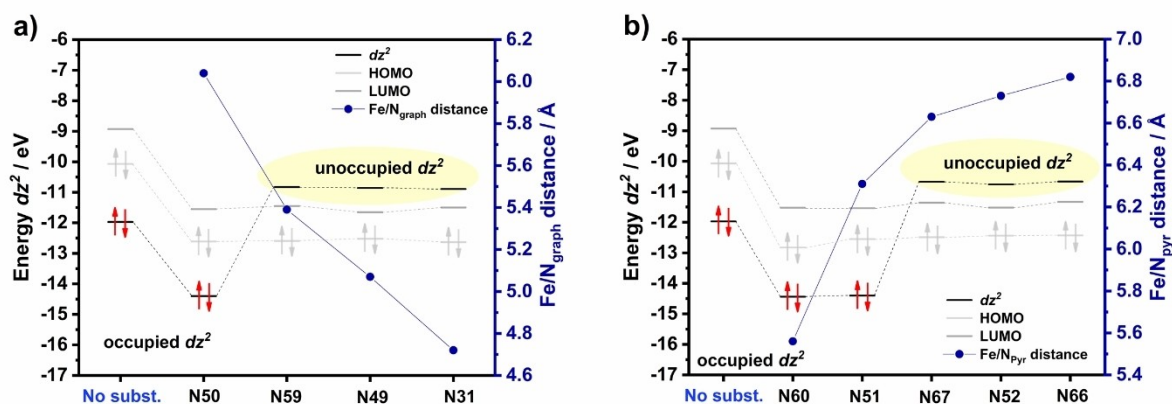


Figure 8. The energy and occupancy perturbation for the dz^2 orbitals in (a) N_{graph} and (b) N_{pyr} models, correlated with the Fe/N distance. In each graph the abscissa coordinate indicates the code number that represents the C atoms for the different optimized models into which a N function was added to the Fe^{II}N4C10 model, in accordance with Figure 7a and 7b.

calculation was done considering that the adduct Fe–O₂ formation is the *r.d.s.* for the ORR on the pyrolyzed catalysts presented in this work. The correlation between the E_{ad} and the iron charge (or iron acidity degree) shown in Figure 9a includes three mixed models with both N_{pyr} and N_{graph} functions, N67_{pyr}/N31_{graph}, N52_{pyr}/N49_{graph} and N66_{pyr}/N59_{graph} (for the rest of the possible mixed N_{pyr}/N_{graph} models the Fe–O₂ affinity is lost with Fe–O distances > 2.7 Å, hence not considered in the results). The obtained correlation of Figure 9a shows a volcano

tendency, explained by the isodensity surfaces of the spin density also included in Figure 9a, that allows mapping the SOMO's 3D shapes of the Fe–O₂ adduct^[83] and thus, depicts the electronic density exchange promoted in the adduct. To a better understanding of this analysis, it is important to recall that the spin density exchange in a molecule can occur by two mechanisms, spin polarization and spin delocalization,^[83] that depending on the predominance of one or another, can be interpreted as the covalency degree of a bonding (the more

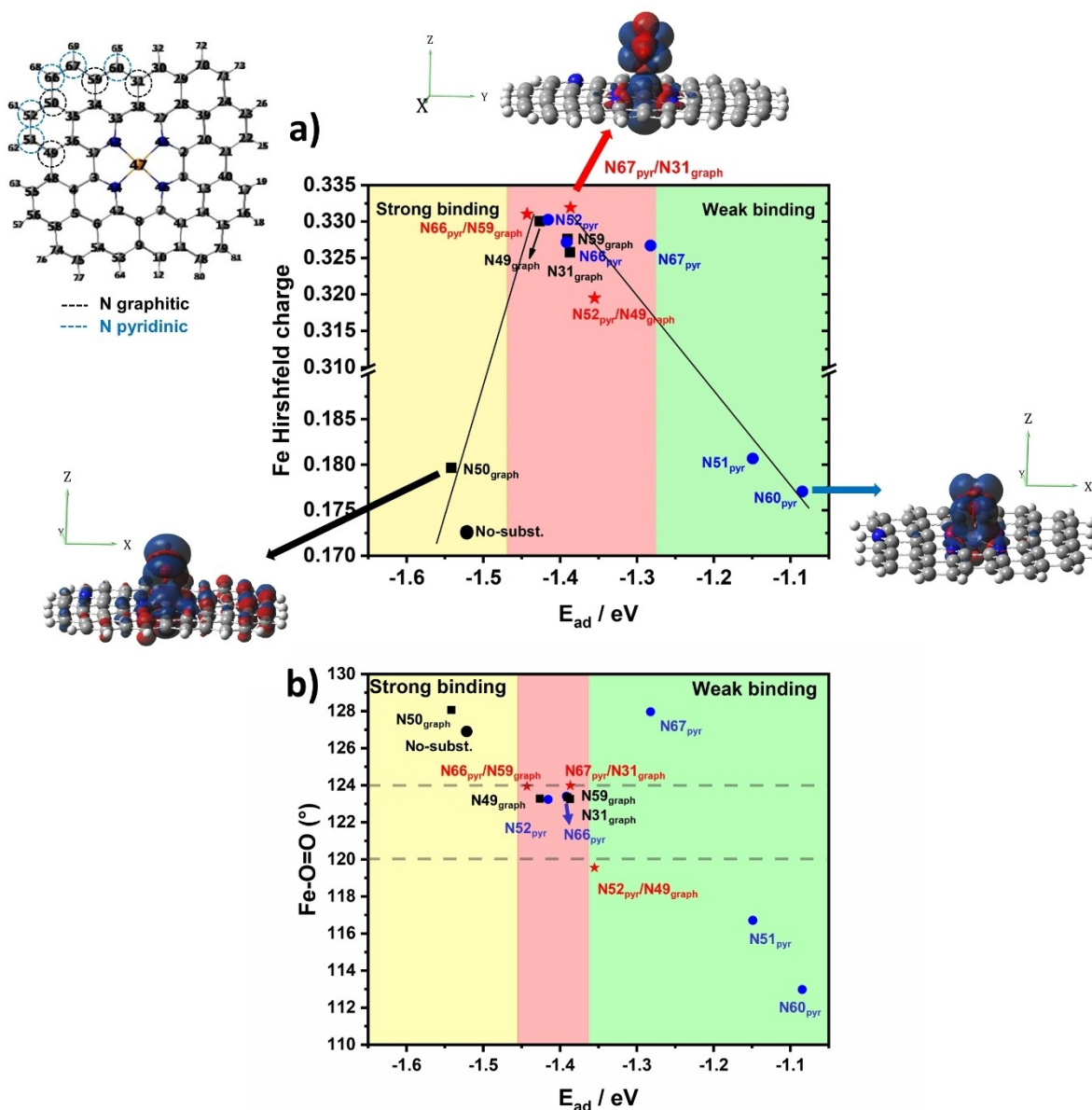


Figure 9. a) Volcano correlation of the calculated Fe–O=O adsorption energies (E_{ad}) with the Fe Hirshfeld charge computed for the different Fe^{II}N₄C₁₀ models having pyridinic and/or graphitic nitrogen functions at varied Fe/N-functions distances. The spin density distribution is depicted for three models: $N50_{graph}$, $N60_{pyr}$, and the mixed model, $N66_{pyr}/N59_{graph}$ (blue and red colors represent positive and negative spin densities, isosurface value = 0.0008 eÅ^{-3}). At the left of the Figure the position of the N substitutions inserted in the Fe^{II}N₄C₁₀ model are shown. The calculation of the E_{ad} was done with the following convention ($E_{ad} = E_{adduct} - (E_{model} + E_{O_2})$), where higher negative values indicate the formation of more stable Fe–O=O adducts. b) Fe–O=O binding angle in function of the calculated adsorption energy (E_{ad}) for the optimized models.

spin delocalization, the more covalent bond). Therefore, for our models, the electron spin exchange analysis allows characterizing the Fe–O donation/back-donation and, therefore, the $dz^2/dxz - \pi_{O=O}/\pi^*_{O=O}$ mixing in the SOMOs of the Fe–O₂ adduct,^[81,82] identifying three regions:

- (i) in the strong binding region (yellow zone), the isodensity surface of the spin density for the $N50_{graph}$ model (as for the *clean* model, see Figure S4) shows that the SOMOs in the Fe–O₂ adduct result from a high spin delocalization (high covalent character) between the oxygen $sp^2-2p\pi$ orbital

and the iron dz^2 frontier orbital, leading to an Fe–O₂ binding with a high σ -character.

- (ii) in the weak binding region (green zone), the spin density distribution for the $N60_{pyr}$ -pyridinic model (as for the $N51_{pyr}$ model) evidences that the SOMOs of the Fe–O₂ adduct also results from a spin delocalization (high covalent character) but now arising between the $sp^2-2p\pi^*$ from the oxygen and the dxz empty orbital from the Fe center leading to a high π -character, with less symmetry than the σ -type binding observed in the region (i).

(iii) for models positioned on the top of the volcano (central red region), the spin density distribution shows that the electronic exchange of the Fe–O₂ adduct results from a spin polarization induced by the $sp^2-2p\pi^*$ orbital of the O₂ molecule to the Fe dz^2 orbital (see N67_{pyr}/N31_{graph} mixed model, Figure 9a and S5). Contrary to the above-described zones (i) and (ii), there is a high predominance of the spin polarization over the spin delocalization, indicating a lower covalent character for Fe–O₂ binding with a dominantly electrostatic character. This interaction along with the highly acid character of the iron centers (high Fe Hirshfeld charge), leads to a synergetic effect that can be interpreted as a potential higher ORR activity.^[37,40,77]

Even though N67_{pyr} and N52_{pyr}/N49_{graph} models fall into the central region of the volcano correlation, the analysis of their spin densities isosurfaces evidenced for these models that the Fe–O₂ adducts exhibit a more covalent interaction (high spin delocalization, Figure S4) falling out from the central red zone (iii) above described. To explain this, we cannot forget the importance of the *end-on* bent M–O=O angle close to 120° for the availability of the O- sp^2 orbital in the Fe–O₂ electronic interaction.^[81,82] Hence, an additional analysis concerning the metric data obtained for the Fe–O=O angle was performed for all the calculated models. Figure 9b depicts the Fe–O=O angles computed in function of the E_{ad} . As it can be observed, the models located near the top of the volcano correlation (red zone (iii) in Figure 9a) exhibit an Fe–O=O angle between 120° and 124°. Nevertheless, the Fe–O=O angles for N67_{pyr} and N52_{pyr}/N49_{graph} models are 128° and 119°, respectively, falling out from this “optimal” range. The models located in the strong- and weak-binding zones also show angles out of this “optimal” range. Therefore, these results demonstrate the importance of the symmetric arrangement for the O₂ molecule over the Fe center since the oxygen SOMO $2p-\pi^*$ requires forming a bond angle of 120° with the Fe active site to establish the binding.^[81] Through the DFT analysis, we demonstrate that this angle depends on the structural and electronic surrounding of the iron center, modulated by the N-functionalities as their proximity to the iron center in our calculated Fe^{II}N4C10 models. For our catalysts Fe-PANI-NP, and Fe-PANI@NP, which experimental $N_{pyr}:N_{graph}$ ratios (Figure 6c) evidences the importance of the synergy of the inserted pyridinic and graphitic nitrogen functions in the catalysis performance. Nevertheless, the ORR catalytic activity will not only depends on the N-inserted functions and their relative positions (Fe/N distances) but also on their combined effect over the iron acidity, the dz^2 iron-orbital energy and occupancy, the Fe–O₂ adsorption energy, the Fe–O₂ binding orbital symmetry, and the Fe–O₂ angle, being thus crucial electronic-structural factors for the optimized orbital iron-oxygen mixing and therefore, for the optimal Fe–O₂ adduct formation to maximizes the ORR catalysis.

Conclusion

Fe–N–C catalysts series were synthesized using Fe₃O₄ nanoparticles as templates and iron source. The NPs play a

fundamental role in generating D1 active sites (Fe^{II}N4 low-spin). The addition of Fe³⁺ as an additional iron source induces the formation of D2 sites along with D1 sites, as was observed for Fe-PANI and Fe-PANI-NP. However, for Fe-PANI@NP, in which the covered NPs are present in the final structure, only the D1 active sites are developed. The Fe-PANI@NP catalyst exhibits a remarkable onset potential of 0.85 V (vs. RHE) in acid media.

On the other hand, the presence of the Fe₃C in the carbonaceous matrix is detrimental for the mechanism since the selectivity change from a direct 4e[−] to a 2×2e[−] mechanism when the amount of Fe₃C increases. We found a positive linear correlation between the $E^{o'} \text{ Fe(III)/Fe(II)}$ redox potential of the catalysts and the ORR onset potential, the catalyst with the highest redox potential present the lower $N_{pyr}:N_{graph}$ ratio, that is, the presence of N-moieties change the electronic structure of the active site and hence the catalytic activity. By DFT calculation, we corroborate the effect of the $N_{pyr}:N_{graph}$ ratio and their distances to the active site on the Fe–O₂ binding in terms of the electronic exchange, orbital mixing, and symmetry. Based on these results, we propose a theoretical model for increasing the activity according to the distance and ratio of N-doped to iron center.

Acknowledgements

This work was supported by Fondecyt Regular Project 1161117, Conicyt Scholarship 21160212, Fondecyt Postdoctoral Projects 3180509 and 3170330, and Anillo Project ACT-192175. By MICIN grant PGC2018-095642-B-I00, MCIN/AEI/10.13039/501100011033 RTI2018-095303-B-C51, by ERDF A way to making Europe, and by CISC grant 2021AEP056. The authors acknowledge Jonathan Urrea for its technical support in the electrochemical studies.

Conflict of Interest

The authors declare no conflict of interest.

Data Availability Statement

Research data are not shared.

Keywords: DFT • Iron Carbides Mechanism • Oxygen Reduction Reaction • Pyrolyzed Electrocatalysts

- [1] U. Martinez, S. Komini Babu, E. F. Holby, H. T. Chung, X. Yin, P. Zelenay, *Adv. Mater.* **2019**, *31*, 1806545.
- [2] M. A. Cropper, S. Geiger, D. M. Jollie, *J. Power Sources* **2004**, *131*, 57–61.
- [3] B. C. H. Steele, A. Heinzl, *Nature* **2001**, *414*, 345–352.
- [4] H. A. Gasteiger, S. S. Kocha, B. Sompalli, F. T. Wagner, *Appl. Catal. B* **2005**, *56*, 9–35.
- [5] S. T. Thompson, D. Papageorgopoulos, *Nat. Catal.* **2019**, *2*, 558–561.
- [6] S. Gupta, D. Tryk, I. Bae, W. Aldred, E. Yeager, *J. Appl. Electrochem.* **1989**, *19*, 19–27.
- [7] G. Wu, P. Zelenay, *Acc. Chem. Res.* **2013**, *46*, 1878–1889.

- [8] E. Proietti, F. Jaouen, M. Lefèvre, N. Larouche, J. Tian, J. Herranz, J. P. Dodelet, *Nat. Commun.* **2011**, 2, DOI 10.1038/ncomms1427.
- [9] G. Wu, K. L. More, C. M. Johnston, P. Zelenay, *Science* **2011**, 332, 443–447.
- [10] A. Serov, M. H. Robson, B. Halevi, K. Artyushkova, P. Atanassov, *Electrochem. Commun.* **2012**, 22, 53–56.
- [11] F. Jaouen, J. Herranz, M. Lefèvre, J. Dodelet, I. Ulrike, U. I. Kramm, I. Herrmann, P. Bogdanoff, J. Maruyama, T. Nagaoka, A. Garsuch, J. R. Dahn, T. Olson, S. Pylypenko, P. Atanassov, E. A. Ustinov, *ACS Appl. Mater. Interfaces* **2009**, 1, 1623–1639.
- [12] K. Artyushkova, S. Rojas-Carbonell, C. Santoro, E. Weiler, A. Serov, R. Awais, R. R. Gokhale, P. Atanassov, *ACS Appl. Energ. Mater.* **2019**, 2, 5406–5418.
- [13] X. Wei, X. Luo, N. Wu, W. Gu, Y. Lin, C. Zhu, *Nano Energy* **2021**, 84, 105817.
- [14] K. Artyushkova, A. Serov, S. Rojas-Carbonell, P. Atanassov, *J. Phys. Chem. C* **2015**, 119, 25917–25928.
- [15] U. Tylus, Q. Jia, K. Strickland, N. Ramaswamy, A. Serov, P. Atanassov, S. Mukerjee, *J. Phys. Chem. C* **2014**, 118, 8999–9008.
- [16] Q. Jia, N. Ramaswamy, U. Tylus, K. Strickland, J. Li, A. Serov, K. Artyushkova, P. Atanassov, J. Anibal, C. Gumezi, S. C. Barton, M.-T. Sougrati, F. Jaouen, B. Halevi, S. Mukerjee, *Nano Energy* **2016**, 29, 65–82.
- [17] M. Kim, H. S. Kim, S. J. Yoo, W. C. Yoo, Y.-E. Sung, *J. Mater. Chem. A* **2017**, 5, 4199–4206.
- [18] I. Matanovic, K. Artyushkova, M. B. Strand, M. J. Dzara, S. Pylypenko, P. Atanassov, *J. Phys. Chem. C* **2016**, 120, 29225–29232.
- [19] U. I. Kramm, L. Ni, S. Wagner, *Adv. Mater.* **2019**, 31, 1805623.
- [20] U. I. Kramm, J. Herranz, N. Larouche, T. M. Arruda, M. Lefèvre, F. Jaouen, P. Bogdanoff, S. Fiechter, I. Abs-Wurmbach, S. Mukerjee, J.-P. Dodelet, *Phys. Chem. Chem. Phys.* **2012**, 14, 11673.
- [21] N. Ramaswamy, U. Tylus, Q. Jia, S. Mukerjee, *J. Am. Chem. Soc.* **2013**, 135, 15443–15449.
- [22] W.-J. Jiang, L. Gu, L. Li, Y. Zhang, X. Zhang, L.-J. Zhang, J.-Q. Wang, J.-S. Hu, Z. Wei, L.-J. Wan, *J. Am. Chem. Soc.* **2016**, 138, 3570–3578.
- [23] M. Xiao, J. Zhu, L. Feng, C. Liu, W. Xing, *Adv. Mater.* **2015**, 27, 2521–2527.
- [24] H.-S. Park, S.-B. Han, D.-H. Kwak, J.-H. Han, K.-W. Park, *J. Catal.* **2019**, 370, 130–137.
- [25] U. I. Kramm, I. Herrmann-Geppert, S. Fiechter, G. Zehl, I. Zizak, I. Dorbandt, D. Schmeißer, P. Bogdanoff, *J. Mater. Chem. A* **2014**, 2, 2663–2670.
- [26] H. Zhang, H. T. Chung, D. A. Cullen, S. Wagner, U. I. Kramm, K. L. More, P. Zelenay, G. Wu, *Energy Environ. Sci.* **2019**, 12, 2548–2558.
- [27] T. Y. Burshtein, D. Aias, J. Wang, M. Sananis, E. M. Farber, O. M. Gazit, I. Grinberg, D. Eisenberg, *Phys. Chem. Chem. Phys.* **2021**, 23, 26674–26679.
- [28] C. Zhao, B. Li, J. Liu, Q. Zhang, *Angew. Chem. Int. Ed.* **2021**, 60, 4448–4463; *Angew. Chem.* **2021**, 133, 4496–4512.
- [29] J. H. Kim, Y. J. Sa, H. Y. Jeong, S. H. Joo, *ACS Appl. Mater. Interfaces* **2017**, 9, 9567–9575.
- [30] Z.-S. Wu, S. Yang, Y. Sun, K. Parvez, X. Feng, K. Müllen, *J. Am. Chem. Soc.* **2012**, 134, 9082–9085.
- [31] H. Zhu, S. Zhang, Y.-X. Huang, L. Wu, S. Sun, *Nano Lett.* **2013**, 13, 2947–2951.
- [32] H. Zhou, Y. Yang, S. You, B. Liu, N. Ren, D. Xing, *Biosens. Bioelectron.* **2018**, 122, 113–120.
- [33] S. Kabir, K. Artyushkova, A. Serov, P. Atanassov, *ACS Appl. Mater. Interfaces* **2018**, 10, 11623–11632.
- [34] S. Rojas-Carbonell, K. Artyushkova, A. Serov, C. Santoro, I. Matanovic, P. Atanassov, *ACS Catal.* **2018**, 8, 3041–3053.
- [35] M. Primbs, Y. Sun, A. Roy, D. Malko, A. Mehmood, M.-T. Sougrati, P.-Y. Blanchard, G. Granozzi, T. Kosmala, G. Daniel, P. Atanassov, J. Sharman, C. Durante, A. Kucernak, D. Jones, F. Jaouen, P. Strasser, *Energy Environ. Sci.* **2020**, 13, 2480–2500.
- [36] A. Ferre-Vilaplana, E. Herrero, *Sustain. Energy Fuels* **2019**, 3, 2391–2398.
- [37] L. Zhang, Z. Xia, *J. Phys. Chem. C* **2011**, 115, 11170–11176.
- [38] J. Zhang, C. Zhao, N. Liu, H. Zhang, J. Liu, Y. Q. Fu, B. Guo, Z. Wang, S. Lei, P. Hu, *Sci. Rep.* **2016**, 6, 28330.
- [39] U. N. Maiti, W. J. Lee, J. M. Lee, Y. Oh, J. Y. Kim, J. E. Kim, J. Shim, T. H. Han, S. O. Kim, *Adv. Mater.* **2014**, 26, 40–67.
- [40] N. Yang, L. Li, J. Li, W. Ding, Z. Wei, *Chem. Sci.* **2018**, 9, 5795–5804.
- [41] J. H. Zagal, S. Griveau, J. F. Silva, T. Nyokong, F. Bedioui, *Coord. Chem. Rev.* **2010**, 254, 2755–2791.
- [42] C. H. Choi, H.-K. Lim, M. W. Chung, G. Chon, N. Ranjbar Sahraie, A. Altin, M.-T. Sougrati, L. Stievano, H. S. Oh, E. S. Park, F. Luo, P. Strasser, G. Dražić, K. J. J. Mayrhofer, H. Kim, F. Jaouen, *Energy Environ. Sci.* **2018**, 11, 3176–3182.
- [43] D. Grasseschi, W. C. Silva, R. de Souza Paiva, L. D. Starke, A. S. do Nascimento, *Coord. Chem. Rev.* **2020**, 422, 213469.
- [44] H. Kim, K. Lee, S. I. Woo, Y. Jung, *Phys. Chem. Chem. Phys.* **2011**, 13, 17505.
- [45] W. Wang, Q. Jia, S. Mukerjee, S. Chen, *ACS Catal.* **2019**, 9, 10126–10141.
- [46] D. Guo, R. Shibuya, C. Akiba, S. Saji, T. Kondo, J. Nakamura, *Science* **2016**, 351, 361–365.
- [47] I. Lozano, N. Casillas, C. P. de León, F. C. Walsh, P. Herrasti, *J. Electrochem. Soc.* **2017**, 164, D184–D191.
- [48] S.-J. Tang, A.-T. Wang, S.-Y. Lin, K.-Y. Huang, C.-C. Yang, J.-M. Yeh, K.-C. Chiu, *Polym. J.* **2011**, 43, 667–675.
- [49] C. Zhu, F. Liu, L. Song, H. Jiang, A. Li, *Environ. Sci.-Nano* **2018**, 5, 487–496.
- [50] R. A. Brand, *Nucl. Instrum. Methods Phys. Res. Sect. B Beam Interact. Mater. Atoms* **1987**, 28, 398–416.
- [51] L. R. F. Allen, J. Bard, *Electrochemical Methods: Fundamentals and Applications*, WILEY, **2000**.
- [52] Gaussian16 (Revision B.01), M. J. Frisch, G. W. Trucks, H. B. Schlegel, G. E. Scuseria, M. A. Robb, J. R. Cheeseman, G. Scalmani, V. Barone, G. A. Petersson, H. Nakatsuji, M. C. X. Li, A. Marenich, J. Bloino, B. G. Janesko, R. Gomperts, B. Mennucci, H. P. Hratchian, J. V. Ortiz, A. F. Izmaylov, J. L. Sonnenberg, D. Williams-Young, F. Ding, F. Lipparini, F. Egidi, J. Ogliaro, M. Bearpark, J. J. Heyd, E. Brothers, K. N. Kudin, V. N. Staroverov, T. Keith, R. Kobayashi, J. Normand, K. Raghavachari, A. Rendell, J. C. Burant, S. S. Iyengar, J. Tomasi, M. Cossi, J. M. Millam, M. Klene, C. Adamo, R. Cammi, J. W. Ochterski, R. L. Martin, K. Morokuma, O. Farkas, J. B. Foresman, D. J. Fox, **2016**.
- [53] C. Adamo, V. Barone, *J. Chem. Phys.* **1999**, 110, 6158–6170.
- [54] A. Schäfer, H. Horn, R. Ahlrichs, *J. Chem. Phys.* **1992**, 97, 2571–2577.
- [55] S. Grimme, S. Ehrlich, L. Goerigk, *J. Comput. Chem.* **2011**, 32, 1456–1465.
- [56] E. R. Davidson, S. Chakravorty, *Theor. Chim. Acta* **1992**, 83, 319–330.
- [57] K. Muñoz-Becerra, R. Venegas, L. Duque, J. H. J. H. Zagal, F. J. F. J. Recio, *Curr. Opin. Electrochem.* **2020**, 23, 154–161.
- [58] T. Herranz, S. Rojas, F. Perez-Alonso, M. Ojeda, P. Terreros, J. Fierro, *J. Catal.* **2006**, 243, 199–211.
- [59] N. D. Leonard, S. Wagner, F. Luo, J. Steinberg, W. Ju, N. Weidler, H. Wang, U. I. Kramm, P. Strasser, *ACS Catal.* **2018**, 8, 1640–1647.
- [60] A. Zitolo, V. Goellner, V. Armel, M.-T. Sougrati, T. Mineva, L. Stievano, E. Fonda, F. Jaouen, *Nat. Mater.* **2015**, 14, 937–942.
- [61] L. Zhong, C. Frandsen, S. Mørup, Y. Hu, C. Pan, L. N. Cleemann, J. O. Jensen, Q. Li, *Appl. Catal. B* **2018**, 221, 406–412.
- [62] Y. Hu, J. O. Jensen, W. Zhang, L. N. Cleemann, W. Xing, N. J. Bjerrum, Q. Li, *Angew. Chem. Int. Ed.* **2014**, 53, 3675–3679; *Angew. Chem.* **2014**, 126, 3749–3753.
- [63] A. Khannanov, A. Kiamov, A. Valimukhametova, D. A. Tayurskii, F. Börrnert, U. Kaiser, S. Eigler, F. G. Vagizov, A. M. Dimiev, *J. Am. Chem. Soc.* **2018**, 140, 9051–9055.
- [64] U. I. Kramm, I. Herrmann-Geppert, P. Bogdanoff, S. Fiechter, *J. Phys. Chem. C* **2011**, 115, 23417–23427.
- [65] U. I. Kramm, M. Lefèvre, N. Larouche, D. Schmeisser, J.-P. Dodelet, *J. Am. Chem. Soc.* **2014**, 136, 978–985.
- [66] T. Mineva, I. Matanovic, P. Atanassov, M.-T. Sougrati, L. Stievano, M. Clémancey, A. Kochem, J.-M. Latour, F. Jaouen, *ACS Catal.* **2019**, 9, 9359–9371.
- [67] M. T. Sougrati, V. Goellner, A. K. Schuppert, L. Stievano, F. Jaouen, *Catal. Today* **2016**, 262, 110–120.
- [68] G. A. Ferrero, K. Preuss, A. B. Fuertes, M. Sevilla, M. M. Titirici, *J. Mater. Chem. A* **2016**, 4, 2581–2589.
- [69] J. H. Zagal, M. T. M. Koper, *Angew. Chem. Int. Ed.* **2016**, 55, 14510–14521; *Angew. Chem.* **2016**, 128, 14726–14738.
- [70] C. Zúñiga, C. Candia-Onfray, R. Venegas, K. Muñoz, J. Urra, M. Sánchez-Arenillas, J. F. Marco, J. H. Zagal, F. J. Recio, *Electrochem. Commun.* **2019**, 102, 78–82.
- [71] A. L. Ward, L. Elbaz, J. B. Kerr, J. Arnold, *Inorg. Chem.* **2012**, 51, 4694–4706.
- [72] E. C. M. Tse, D. Schilter, D. L. Gray, T. B. Rauchfuss, A. A. Gewirth, *Inorg. Chem.* **2014**, 53, 8505–8516.
- [73] R. Venegas, K. Muñoz-Becerra, C. Candia-Onfray, J. F. Marco, J. H. Zagal, F. J. Recio, *Electrochim. Acta* **2020**, 332, 135340.
- [74] S. Gupta, C. Fierro, E. Yeager, *J. Electroanal. Chem. Interfacial Electrochem.* **1991**, 306, 239–250.

- [75] S. Specchia, P. Atanassov, J. H. Zagal, *Curr. Opin. Electrochem.* **2021**, *27*, 100687.
- [76] K. Kumar, L. Dubau, M. Mermoux, J. Li, A. Zitolo, J. Nelayah, F. Jaouen, F. Maillard, *Angew. Chem.* **2020**, *132*, 3261–3269; *Angew. Chem. Int. Ed.* **2020**, *59*, 3235–3243.
- [77] X. Ning, Y. Li, J. Ming, Q. Wang, H. Wang, Y. Cao, F. Peng, Y. Yang, H. Yu, *Chem. Sci.* **2019**, *10*, 1589–1596.
- [78] O. S. Trofymchuk, D. E. Ortega, S. Gutiérrez-Oliva, R. S. Rojas, A. Toro-Labbé, *J. Mol. Model.* **2015**, *21*, 227.
- [79] K. Muñoz-Becerra, D. F. Báez, J. H. Zagal, S. Bollo, A. Toro-Labbé, R. Venegas, F. J. Recio, *Electrochim. Acta* **2020**, *357*, 0–3.
- [80] J. S. Bertini, Ivano, Gray, Harry B. Lippard, Stephen J., Valentine, *Bioinorganic Chemistry*, University Science Books Mill Valley CA, **1994**.
- [81] T. G. Spiro, A. V. Soldatova, G. Balakrishnan, *Coord. Chem. Rev.* **2013**, *257*, 511–527.
- [82] A. Kumar, Y. Zhang, W. Liu, X. Sun, *Coord. Chem. Rev.* **2020**, *402*, 213047.
- [83] E. Ruiz, J. Cirera, S. Alvarez, *Coord. Chem. Rev.* **2005**, *249*, 2649–2660.

Manuscript received: January 31, 2022

Revised manuscript received: February 22, 2022

Accepted manuscript online: March 1, 2022